Received: 9 July 2024 | Revised: 14 September 2024 | Accepted: 30 September 2024

DOI: 10.1002/dro2.148

RESEARCH ARTICLE

Droplet WILEY

Effect of gas flow rate on bubble formation on superhydrophobic surface

Daniel O'Coin | **Hangjian Ling**

Department of Mechanical Engineering, University of Massachusetts Dartmouth, Dartmouth, Massachusetts, USA

Correspondence
Hangjian Ling, Department of Mechanical Engineering, University of Massachusetts Dartmouth, Dartmouth, MA 02747, USA.
Email: hling1@umassd.edu

Funding information
National Science Foundation, Grant/Award Numbers: 2041479, 2339606; Office of Naval Research, Grant/Award Number: N00014-20-1-2170; University of Massachusetts OTCV Technology Development Fund

Abstract

We experimentally studied the effect of gas flow rate Q on the bubble formation on a superhydrophobic surface (SHS). We varied Q in the range of $0.001 < Q/Q_{cr} < 0.35$, where Q_{cr} is the critical value for a transition from the quasi-static regime to the dynamic regime. The bubble geometrical parameters and forces acting on the bubble were calculated. We found that as Q increase, the bubble detached volume (V_d) increased. After proper normalization, the relationship between V_d and Q generally agreed with those observed for bubbles detaching from hydrophilic and hydrophobic surfaces. Furthermore, we found that Q had a minor impact on bubble shape and the duration of bubble necking due to the negligible momentum of injected gas compared to surface tension and hydrostatic pressure. Lastly, we explained the primary reason for the larger V_d at higher flow rates, which was increased bubble volume during the necking process. Our results enhanced the fundamental understanding of bubble formation on complex surfaces and could provide potential solutions for controlling bubble generation and extending the application of SHS for drag reduction, anti-fouling, and heat and mass transfer enhancement.

INTRODUCTION

The formation of a gas bubble on a solid surface submerged in the liquid has received great attention due to its importance in many industrial and biomedical applications, including particle separation,[1] surface cleaning,[2] and drug delivery.[3,4] Within these applications, predicting and controlling the volume of detached bubble (V_d) is important because the bubble size determines the gas–liquid interfacial area and thereby the amount of heat and mass transfer across the interface.[5,6] The simplest way to create a bubble is probably by injecting gas through an orifice created on the surface. Previous studies have investigated the change in V_d due to various factors, including the size and shape of the orifice,[7–9] the wetting properties and contact angle of the solid surface,[10–14] the conditions and flow rate of gas injection,[15–17] and the properties of the liquid.[18,19] Numerous studies focused on the bubble formation through micro-orifices with an aim to reduce the bubble size.[20] Recently, there is a growing interest on the bubble formation by injecting gas through an orifice made on superhydrophobic surface (SHS).[21–24] The SHS is a material inspired by the lotus leaf and is created by a combination of surface roughness and hydrophobic chemistry.[25,26] The SHS is distinct from hydrophobic surfaces due to its large static contact angle (SCA), low contact angle hysteresis, and the presence of a thin gas layer within the surface roughness when submerged in the liquid. Considering the wide applications of SHS, such as drag reduction,[27–30] heat transfer enhancement,[31–34] anti-bacteria,[35,36] anti-icing,[37,38] and anti-corrosion,[39,40] understanding the dynamics of bubble formation on SHS could have significant impacts. For example, it may provide new strategies for sustaining the gas layer on SHS when subjected to turbulent flows[41] or gas diffusion.[42,43]

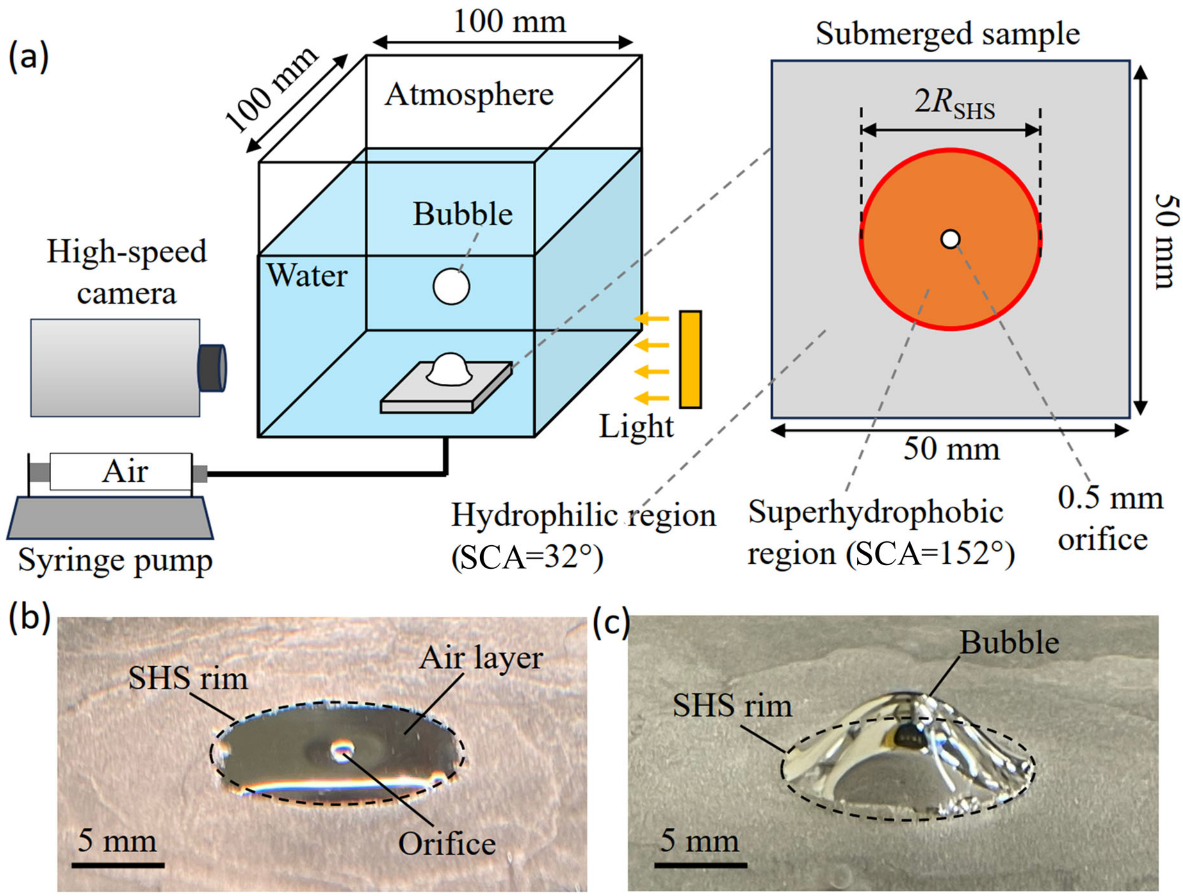

FIGURE 1 Experimental setup for studying bubble formation on superhydrophobic surface (SHS). (a) A schematic drawing of the experimental setup (SCA means static contact angle of the surface). (b) An image showing the presence of air layer on the SHS when submerged in water. (c) An image showing a growing bubble on SHS with a bubble base pinning at the rim of SHS.

A few experimental studies[21–24] have measured the formation of a bubble by injecting gas through an orifice on SHS at low gas flow rates ($Q < 10$ mL/min). Rubio-Rubio et al.[21] found that as there is increase in the radius of SHS (R_{SHS}), the bubble formation transitioned from mode A, where the bubble base was fixed at the rim of SHS, to mode B, where the contact line moved on the horizontal surface and did not reach the SHS boundary. They also showed that both bubble shape and V_d could be predicted by solving the Young–Laplace equation with certain boundary conditions. Qiao et al.[22] calculated the tangential force that constrained the spread of bubble from the superhydrophobic region to the hydrophilic region. Breveleri et al.[23] measured the bubble formation on an SHS fabricated on a porous material. They found that the bubble size increased with an increase in the pressure difference on two sides of the porous surface. Recently, O'Coin and Ling[24] calculated the forces acting on a bubble growing on SHS and found a balance between one lifting force (pressure force) and two retaining forces (surface tension force and buoyancy force).

However, the effect of gas flow rate (Q) on the bubble formation on SHS has received less attention, even though Q could play a critical role in the size of detached bubble. For example, for a bubble forming from a nozzle, previous studies[6,16,44] showed that increasing Q caused a transition from the quasi-static bubble growing regime to the dynamic regime, along with a significant increase of V_d. However, it remains unclear whether Q has a similar effect for bubble formation on SHS. This paper aims to address this knowledge gap by experimentally measuring the bubble formation on SHS at various gas flow rates. We will examine the effect of Q on the detached bubble size, bubble geometrical parameters, necking process, as well as forces acting on the bubble. We will show that V_d increases with increasing Q and follows a relation similar to those reported in the literature. Moreover, we will explain the primary reason for a larger V_d, which is the increased volume during the bubble necking process.

RESULTS AND DISCUSSION

Figure 1a shows the experimental setup. An SHS with a radius R_{SHS} is submerged in water with a density of $\rho_L = 997$ kg/m^3. An air bubble with a density of $\rho_G = 1.2$ kg/m^3 forms on the SHS. Air is supplied to the bubble at a constant flow rate using a syringe pump. The bubble shape is recorded by a high-speed camera with a maximum frame rate of 1000 frames per second. The SCA of the SHS is 152°. Before a bubble forms, a uniform air layer is present on the submerged SHS (Figure 1b). When a bubble forms, the bubble base either pins to the rim of SHS for small R_{SHS} (Figure 1c) or moves on the SHS without reaching the SHS rim for sufficiently large R_{SHS}.

TABLE 1 Main experimental parameters and results in current study.

R_{SHS} (mm)	R_b^{max}(mm)	Q (mL/min)	Q/Q_{cr}	V_d (mL)
4.2	4.2	1–150	0.0023–0.35	0.17–0.29
6.3	6.3	1–150	0.0016–0.25	0.30–0.43
19.0	7.2–7.9	1–150	0.0071–0.21	0.34–0.58

Table 1 lists the main experimental parameters. Three different R_{SHS} of 4.2, 6.3, and 19.0 mm and five different gas flow rates (Q) of 1, 5, 20, 50, and 150 mL/min are considered in this study. For R_{SHS} = 4.2 and 6.3 mm, the bubble base is fixed at the rim of SHS so the maximum bubble base radius is $R_b^{max} = R_{SHS}$. For R_{SHS} = 19.0 mm, the bubble base does not reach the SHS boundary so that $R_b^{max} < R_{SHS}$, and R_b^{max} varies slightly at different flow rates. We expect that results for an infinite R_{SHS} will be similar to those observed for R_{SHS} = 19.0 mm. The effect of Q on bubble formation is similar for different R_{SHS}. In the following, we will mainly show results obtained for R_{SHS} = 6.3 mm. Results for R_{SHS} = 4.2 and 19.0 mm can be found in the Supporting Information.

Table 1 also provides the range of Q/Q_{cr}, where Q_{cr} is the critical flow rate for the transition from the quasi-static regime to the dynamic regime. Following Oguz and Prosperetti[16] and Rubio-Rubio et al.,[21] Q_{cr} is calculated as: $Q_{cr} = \pi(16/3g^2)^{1/6}(\sigma R_b^{max}/\rho_L)^{5/6}$, where $\sigma = 72$ mN/m is the surface tension and $g = 9.78$ m^2/s is the gravitational acceleration. In the current study, Q/Q_{cr} does not exceed 0.35. Similarly, the Weber number $We = \rho_L Q^2/\pi\sigma R_b^{max\,3}$ (ratio of gas momentum to surface tension) does not exceed 0.12. Due to the small values of Q and We, we will show later that the dynamic forces due to the momentums of injected gas and surrounding liquid are negligible, and the gas flow rate has a minor impact on the bubble shape. Nevertheless, we will show that V_d increases as increasing Q.

Figure 2 shows the evolution of bubble shape over time (t) on SHS with R_{SHS} = 6.3 mm and for five different flow rates. Figure 3 shows the effects of Q on the bubbling period T_0, the time duration of necking (or the time from the appearance of a neck on the bubble to the bubble detachment) T_n, and V_d. The evolutions of bubble shape for R_{SHS} = 4.2 and 19.0 mm are shown in Supporting Information: Figures S1 and S2, respectively. Time t = 0 is defined as the time of detachment of the previous bubble. Clearly, for different flow rates, the bubble shape undergoes a similar evolution (Figure 2, Supporting Information: Figures S1 and S2), and the time duration of necking is nearly same $T_n \sim 20$ ms (Figures 2 and 3a). These results indicate that the bubble shape and the bubble necking are not affected by the momentum of the injected gas. Nevertheless, as increasing Q, T_0 decreases (Figure 3a) and thereby T_n/T_0 (the percentage of necking duration to the bubbling period) increases from <1% to ~20%. Moreover, V_d increases by 1.4–1.7 times as increasing Q from 1 to 150 mL/min (Figures 2 and 3b).

Figure 3c shows V_d/V_T as a function of Q/Q_{cr}. Here, $V_T = 2\pi R_b^{max}\sigma/\rho_L g$ is the Tate volume[45] derived from the balance between

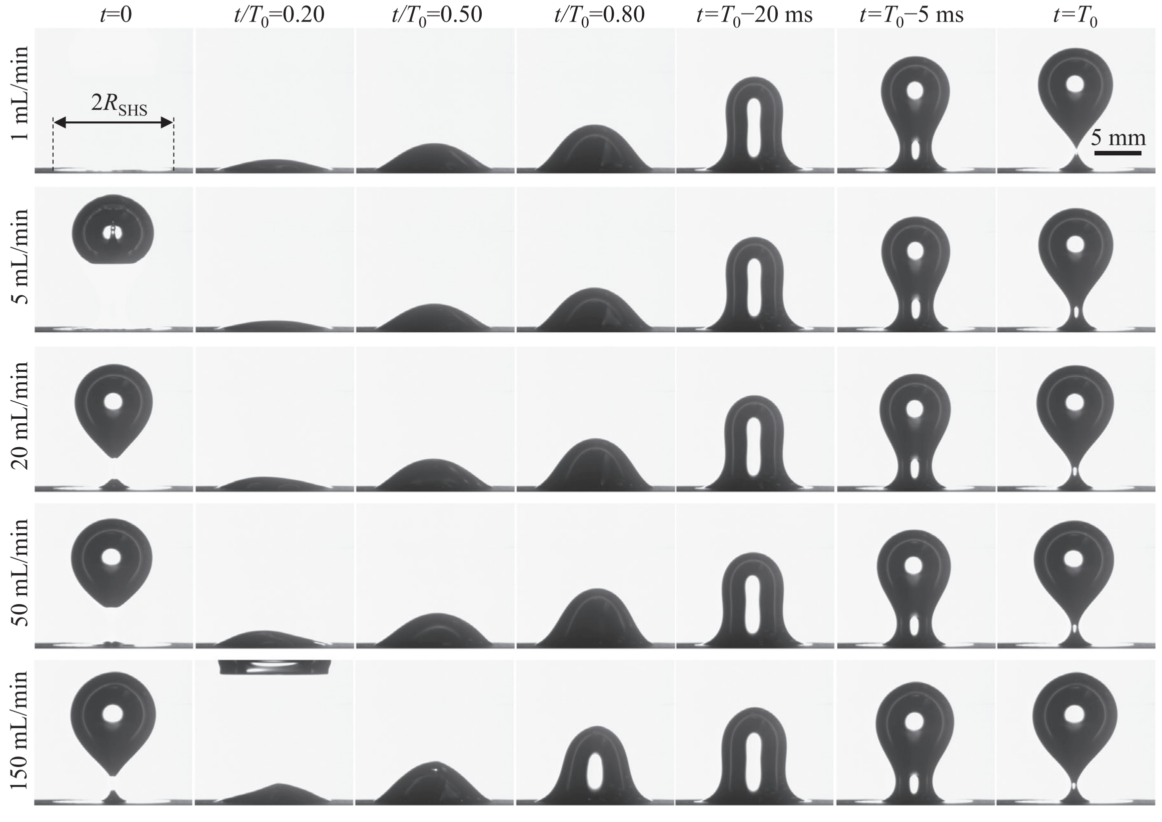

FIGURE 2 Time-evolutions of bubble shape at five different gas flow rates. Results are obtained for superhydrophobic surface (SHS) with R_{SHS} = 6.3 mm. Time t = 0 is defined as the time of detachment of previous bubble, and T_0 is the bubbling period. Results for R_{SHS} = 4.2 mm and 19.0 mm are shown in Supporting Information: Figures S1 and S2, respectively.

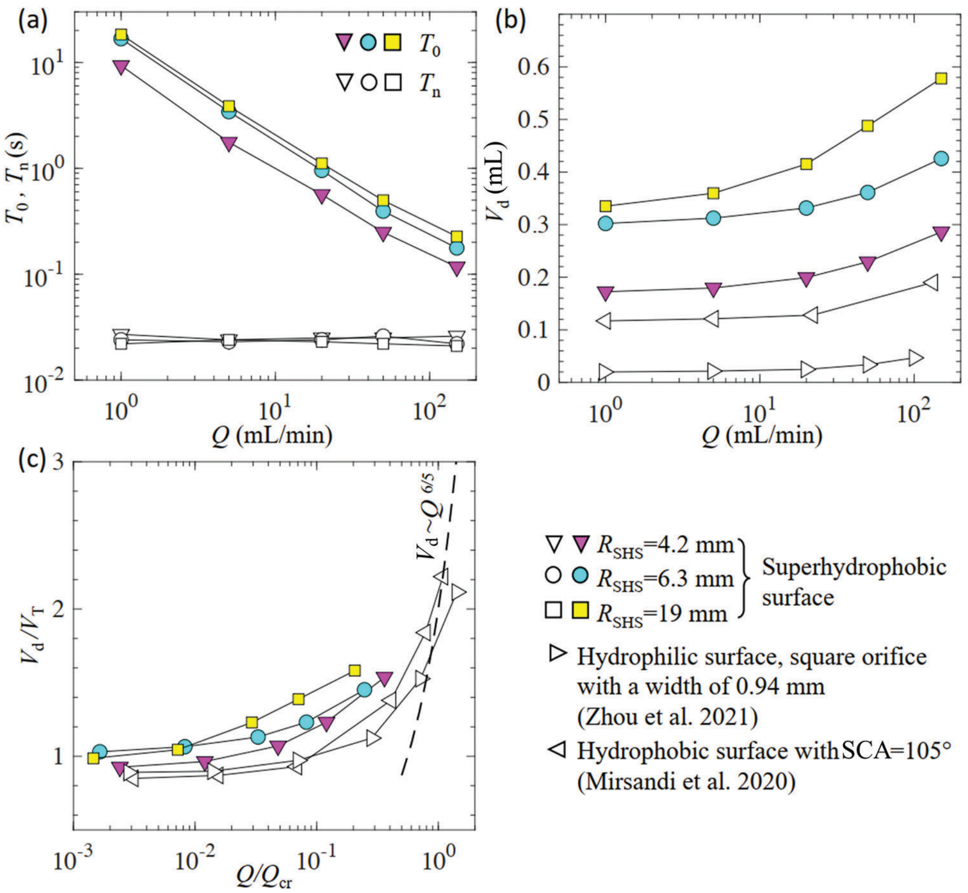

FIGURE 3 Effect of gas flow rate on bubbling period and bubble detached volume. (a) Bubbling period (T_0) and necking duration (T_n) as a function of Q. (b) Detached bubble volume (V_d) as a function of Q. (c) V_d/V_T as a function of Q/Q_{cr}, where Q_{cr} is the critical flow rate for the transition from the quasi-static regime to the dynamic regime.

surface tension and buoyancy. For comparison, results for bubble formation on a hydrophobic surface[14] and a hydrophilic surface[7] are also plotted. As shown in Figure 3b, surface wettability has a significant effect on V_d. The SHS has the largest V_d compared to hydrophilic and hydrophobic surfaces. This result is consistent with the simulations,[12] which show that V_d increases as increasing the SCA of the surface. However, as shown in Figure 3c, after normalization, regardless of the surface type, the profiles generally follow the same trends. For sufficiently low flow rates ($Q \ll Q_{cr}$), V_d/V_T is close to 1, suggesting that the bubble is governed by a balance between surface tension and hydrostatic pressure. However, as Q approaches Q_{cr}, V_d/V_T increases and is larger than 1. For sufficiently large Q and for bubble detaching from a nozzle and from hydrophobic and hydrophilic surfaces, previous studies[13,14,16] showed a power-law relation $V_d \sim Q^{6/5}$. Due to the limited range of Q in the current study, we leave the relation between V_d and Q in the dynamic regime ($Q > Q_{cr}$) for future work.

In the following, we will discuss the effect of Q on the bubble geometrical parameters, the bubble necking process, as well as the forces acting on the bubble. We aim to understand the reason why the bubble size increases as increasing Q.

Figure 4 shows the impact of Q on the variations of bubble geometrical parameters, including bubble height H/l_σ, bubble base radius R_b/l_σ and bubble radius at the apex R_a/l_σ. Figure 4a–c are shown as a function of t/T_0. Figure 4d–f are shown as a function of V/l_σ^3, where V is the bubble volume. Here, the capillary length scale $l_\sigma = (\sigma/\rho_L g)^{0.5} = 2.7$ mm is chosen for normalization. Regardless of Q, the profiles have similar trends: as the bubble grows, H continuously increases, R_b experiences three stages (an initial increase due to the expansion of bubble base, then nearly constant, and final a reduction due to the necking), and R_a reduces continuously until the necking occurs. Moreover, before necking occurs, the profiles at different flow rates overlap nicely when showing as a function of V (Figure 4d–f), consistent with the similar bubble shapes at different flows rates shown in Figure 2. Again, these results suggest that the bubble shape is only a function of V and is not affected by the flow rate. In fact, at low flow rates and in the quasi-static region, previous study[21] has shown that for a bubble growing on SHS, the bubble shape can be estimated by Young–Laplace equation.

Nevertheless, Q has the following three notable effects on these profiles. First, since V_d (i.e., V at $t/T_0 = 1$) increases as increasing Q, a larger Q causes the bubble to reach a certain volume and thereby a certain shape at a smaller t/T_0. For example, as shown in Figure 4a, as increasing Q from 1 to 150 mL/min, the time for bubble to achieve a height of $H/l_\sigma = 2.0$ reduces from $t/T_0 = 0.90$–0.65. Second, as increasing Q, the bubble achieves a larger V at the time when R_b starts

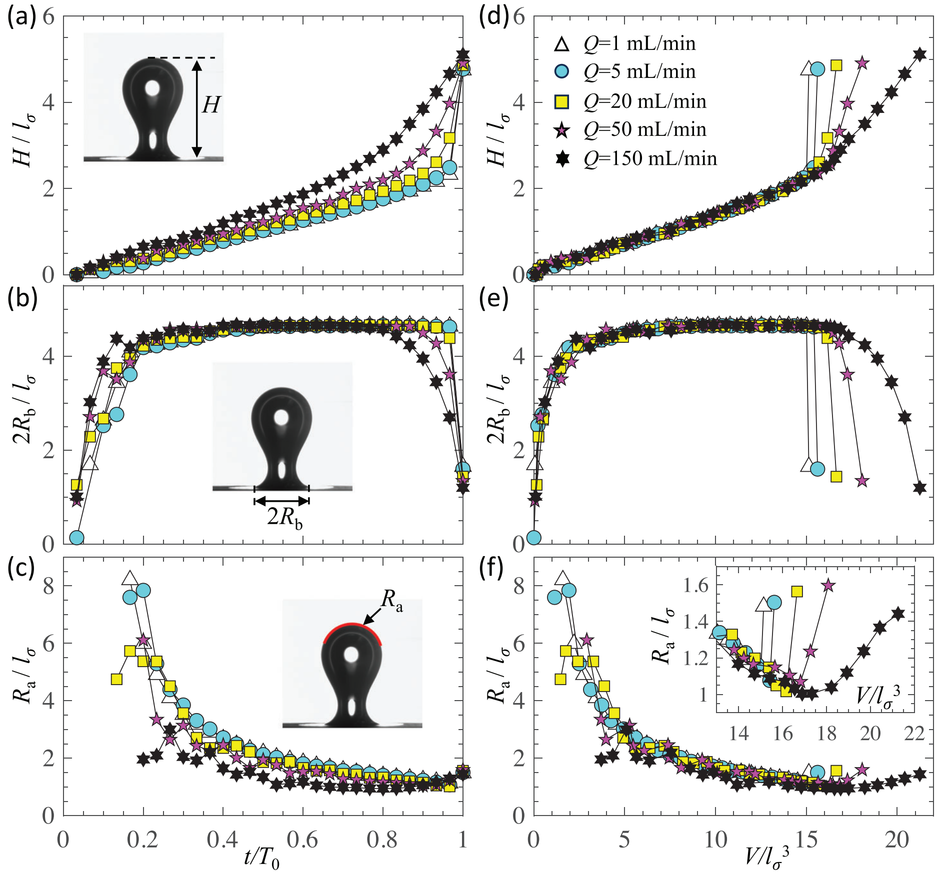

FIGURE 4 Effect of gas flow rate on bubble geometrical parameters. (a–c) Bubble height H/l_σ, bubble base radius R_b/l_σ, and radius at the apex R_a/l_σ as a function of t/T_0. (d–f) Same results shown as a function of bubble volume V/l_σ^3. The capillary length scale l_σ is used for normalization. Results shown are for superhydrophobic surface (SHS) with $R_{SHS} = 6.3$ mm. Results for $R_{SHS} = 4.2$ and 19.0 mm are shown in Supporting Information: Figures S3 and S4, respectively.

to decrease (Figure 4e). This result might indicate that the maximum equilibrium volume V_e (i.e., the volume just before the bubble loses stability) increases as increasing Q. Lastly, Q modifies the trends of profiles during the necking process: the profiles experience a sudden jump for small Q but change smoothly for large Q. This is because, as increasing Q, T_n/T_0 increases (i.e., the percentage of necking duration to the overall bubbling period increases).

Figure 5 shows the effect of Q on the bubble necking process. Clearly, for different flow rates, when plotting results as a function of $t - T_0$, the bubble shape (Figure 5a), bubble geometrical parameters (Figure 5b), bubble vertical acceleration (a_b) (Figure 5c), and the minimal necking radius (R_{neck}) (Figure 5d) exhibit similar time evolutions. Noted that the jump for the curve in Figure 5c ($Q = 150$ mL/min) is due to measurement uncertainty in the bubble acceleration (~0.3 g). Furthermore, the reduction of R_{neck} with respect to time follows a power-law relation $R_{neck} \sim (T_0 - t)^{0.55}$, where the power-law exponent agrees with that for a bubble detaching from a nozzle.[46–49] These results are consistent with the nearly constant T_n, as shown in Figure 3a, further demonstrating that the flow rate has a minor effect the necking process. As explained early, the reason is that the momentum of the injected gas is negligible compared to the surface tension.

Nevertheless, Q affects the variation of bubble volume (Figure 5e). The mechanism behind the increased detached volume with increasing Q can be explained by Figure 5e. During the necking, V is nearly constant for $Q = 1$ mL/min, but increases by a significant amount for $Q = 150$ mL/min. The reason is that the ratio of the volume change during necking (QT_n) to the bubble detached volume ($V_d = QT_0$) is T_n/T_0, which increases from less than 1% to ~20% as increasing Q. Consequently, for different flow rates, the difference in V is small at the beginning of necking process but increases significantly by the end of necking. This result explains why V_d increases as increasing Q.

Figure 6a,b shows the variations of forces acting on the bubble for $Q = 1$ and 150 mL/min, respectively. Following our previous work,[24] we calculated six forces applied on the bubble, including the pressure force $F_P = (2\sigma/R_a+\rho_G gH)\pi R_b^2$ mainly caused by the surface tension at the bubble apex, the gas momentum force $F_{GM} = \rho_G Q^2/\pi R_b^2$ due to the gas injected into the bubble, the surface tension force $F_S = -2\pi R_b \sigma \sin\theta$ applied at the rim of bubble base, as illustrated in Supporting Information: Figure S7 (we assume that the rim of bubble base contacts with the tip of surface texture, θ is the contact angle at rim of bubble base), the buoyancy force $F_B = (\rho_L - \rho_G)gV - \rho_L gH\pi R_b^2$ due to the hydrostatic pressure applied on the bubble surface, the liquid inertia force $F_{LI} = -(11/16\rho_L + \rho_G)(VdU_b/dt + U_b dV/dt)$ accounting for the

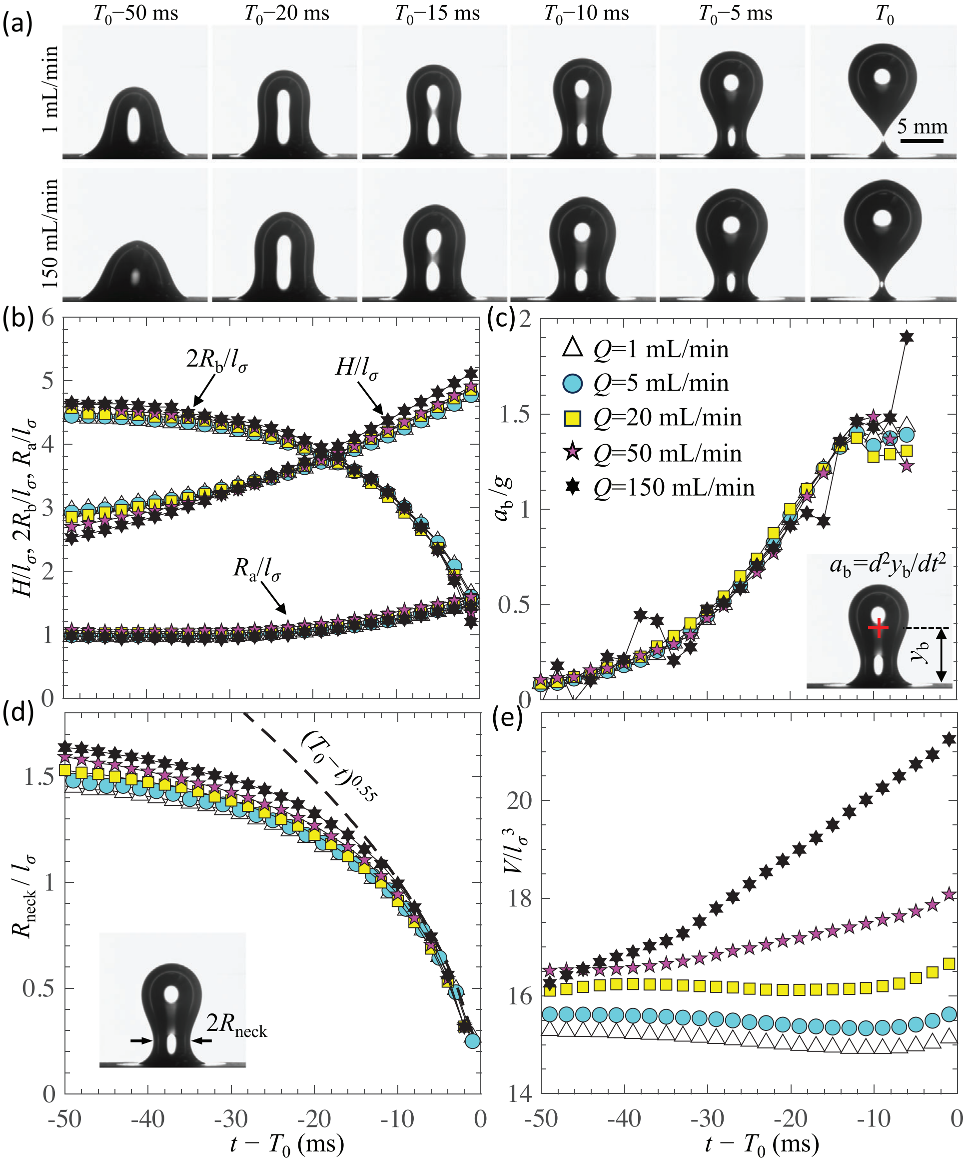

FIGURE 5 Effect of gas flow rate on the bubble necking process. (a) Evolutions of bubble shape at two gas flow rates $Q = 1$ and 150 mL/min. (b) Variations of H/l_σ, R_b/l_σ, and R_a/l_σ as a function of $t - T_0$. (c–e) Variations of vertical acceleration a_b/g (c), minimum neck radius R_{neck}/l_σ (d), and bubble volume V/l_σ^3 (e) as a function of $t - T_0$. Results shown are for $R_{SHS} = 6.3$ mm. Results for $R_{SHS} = 4.2$ and 19.0 mm are shown in Supporting Information: Figures S5 and S6, respectively.

momentum of surrounding liquid, and the drag force $F_D = -1/2\rho_L C_D \pi R_b^2 U_b^2$. Here, a positive value indicates the force is in the upward direction, U_b denotes the velocity of bubble in the vertical direction, C_D is the drag coefficient given by $C_D = 24/Re_b(1 + 0.15Re_b^{0.687})$,[50] where $Re_b = \rho_L U_b R_b/\mu_L$ is the Reynolds number and $\mu_L = 1.0 \times 10^{-3}$ N s/m^2 is the dynamic viscosity of the water.

As shown in Figure 6, for both flow rates, the primary forces acting on the bubble are F_P, which lifts the bubble, and F_B and F_S, which are the two retaining forces. Regardless of flow rates, these forces follow similar trends: both $|F_P|$ and $|F_B|$ increase linearly with the bubble volume, and $|F_S|$ initially increases and then remains constant. As increasing Q, due to the larger V_d, the maximum values of $|F_P|$ and $|F_B|$ increase. Moreover, the sum of these three forces: $F_P + F_B + F_S$ is close to 0. These results confirm that the dynamics forces due to the momentums of the injected gas and the surrounding liquid are negligible compared to the forces due to surface tension and hydrostatic pressure, suggesting that the bubble formation is in the quasi-static regime. This explains why the flow rate has a minor effect on the bubble shape (Figure 3), bubble geomatical parameters (Figure 4), and the bubble necking (Figure 5).

Furthermore, as shown in Figure 6b, during the necking, the buoyancy force acting on the bubble remains negative, suggesting that the positive a_b shown in Figure 5c is due to the contraction of the bubble in the horizontal direction under the action of surface tension. Although the buoyancy force is the main reason for bubble detachment when it is generated from a nozzle or hydrophilic surface,[51,52] this is not the case here. Instead, we believe that bubble necking and detachment on SHS occur because the bubble reaches its maximum equilibrium volume, as

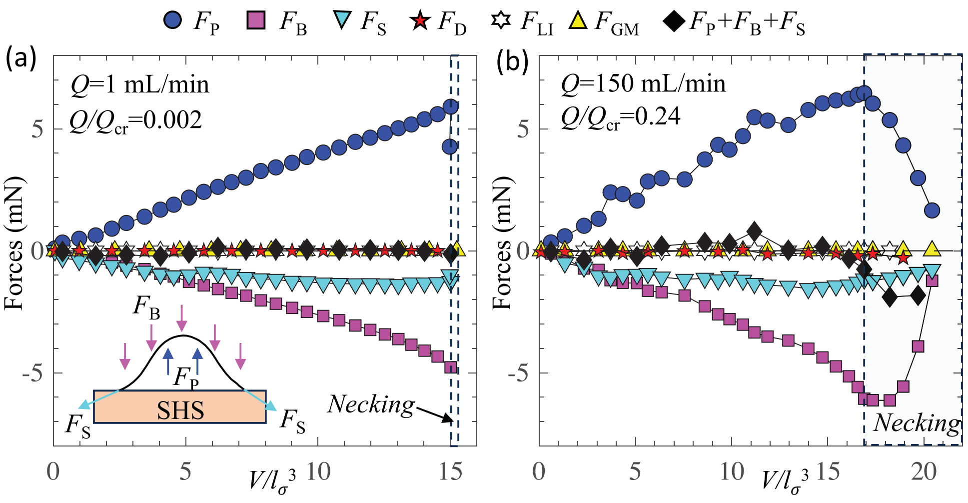

FIGURE 6 Effect of gas flow rate on the forces acting on the bubble. (a and b) Variations of forces acting on the bubble for $Q = 1$ mL/min (a) and $Q = 150$ mL/min (b). Results are obtained for $R_{SHS} = 6.3$ mm. Results for $R_{SHS} = 4.2$ and 19.0 mm follow similar trends and are not shown.

explained by Rubio-Rubio et al.[21] The necking is primarily driven by the surface tension, which minimizes the surface area of the bubble and forces the bubble to shrink in the horizontal direction and expand in the vertical direction.

CONCLUSION

In summary, we studied the effect of gas flow rate on bubble formation on SHS, including bubble detached volume, bubbling period, bubble geometrical parameters, necking process, as well as the forces acting on the bubble. The gas flow rate varied in the range of $1 < Q < 150$ mL/min and $0.001 < Q/Q_{cr} < 0.35$. The main conclusions are listed below:

- *Bubble detached volume*: Although the current flow rates were in the quasi-static regime ($Q < Q_{cr}$), an increased V_d with increasing Q was observed. The increased V_d was mainly due to the increased bubble volume during the necking process. After proper normalization, the relationship between V_d and Q for hydrophilic, hydrophobic, and SHSs generally followed similar trends.
- *Bubble shape and necking*: The flow rate had a minor impact on the bubble shape and the duration of necking due to the small momentum of the injected gas.
- *Forces acting on bubble*: For the current flow rates, the bubble was driven by a balance between one lifting force (pressure force) and two retaining forces (surface tension force and buoyancy force). The dynamics forces caused by the momentums of the injected gas and surrounding liquid were negligible.

Overall, our results enhance the understanding of bubble formation on SHS. Considering the wide applications of SHS, such as drag reduction, anti-bacteria, anti-icing, and anti-corrosion, our findings may have significant impacts. For example, our results may lead to the development of new techniques for restoring the gas layer and thereby maintaining SHS functions for submerged SHS. Our results showed that even though the gas was injected through a single orifice, it could spread along the SHS as the bubble base expanded or retracted (as shown in Figure 4b, the change of R_b). This result may indicate that gas injection through an orifice on SHS may provide a simple solution for restoring the Cassie–Baxter state. In addition, our findings regarding the bubbling period and detached volume provide insights into the amount of gas required to restore the Cassie–Baxter state. Our results could also inspire new methods to control bubble size that involve micro/nano-engineered surfaces.

The current gas flow rates were relatively low and were in the quasi-static regime. Future studies are required to understand the bubble formation process and the detached bubble volume on SHS at higher gas flow rates at the dynamic regime. Future studies are also needed to understand why, for a bubble experiencing a negative buoyancy force during the growing process, the detached volume at low flow rates still shows a good agreement with V_T, which assumes a positive buoyancy force acting on bubble.

METHODS

The experiments were performed in a transparent acrylic tank filled with water. The tank had an inner dimension of 100 mm by 100 mm, and the height of the water was 70 mm. These dimensions were sufficiently larger than the size of the bubble, ensuring a negligible influence on the bubble formation. An SHS with a radius of 4.2 mm $< R_{SHS} <$ 19.0 mm was installed at the bottom of the tank. It was created on a 50 mm by 50 mm aluminum plate. To fabricate the SHS, we first created surface roughness by sandblasting the entire aluminum surface with an abrasive medium of grit size 60 (particle mesh size 35–100). Then, the rough surface was cleaned in an ultrasonic bath and coated with hydrophobic nano-particles (Glaco Mirror Coat Zero, by SOFT99 Corp.). Only the center region with a radius of R_{SHS} was coated. The SCAs on the superhydrophobic and hydrophilic regions were 152 ± 2° and

32 ± 2°, respectively. The sliding angle of a water droplet on the SHS was 5 ± 2°.

To promote the bubble formation on the SHS, a 0.5 mm diameter orifice was fabricated at the center of the SHS. The orifice was manufactured before the deposition of the hydrophobic nano-particles. As a result, during our experiments, the bubble base spread beyond the orifice rim immediately after bubble formation. A syringe pump (model #NE-1010 SyringeONE, by New Era Pump System Inc.) was used to supply gas through the orifice. A long needle with a length of 152 mm and an inner diameter of 0.61 mm was installed below the orifice to ensure that the pressure variation in the bubble did not cause a notable change in the pressure in the syringe. A constant gas flow rate was achieved for all cases, as shown in Supporting Information: Figure S8. The current method of injecting gas through an orifice on the SHS is closely relevant to some practical applications of SHS. For example, a few researchers[53–56] fabricated SHS on a porous base and injected gas through the porous material with an aim to recover the drag reduction properties of SHS in turbulent flows. The current SHS with a single orifice is a simplified model of SHS developed on porous material with many irregular orifices. We believe this simplified model provides a fundamental understanding of bubble dynamics on SHS.

To record the bubble formation, a high-speed camera (PCO.dimax S4, pixel size 11 μm, 2016 × 2016 pixels) and a collimated light (Thorlabs, model #QTH10, power 50 mW) were used. The maximum frame rate used in this study was 1000 frames per second, which provided a sufficient temporal resolution to capture the bubble's growth and necking processes. The spatial resolution of the imaging system was 34 μm/pixel. The data were recorded after a series of bubbles had formed and detached from the surface. The light was turned on only for a short duration of time and did not change the water temperature.

We applied an image processing procedure described in our previous work[24] to measure the bubble geometrical parameters, including the volume (V), base radius (R_b), height (H), radius at the apex (R_a), and contact angle at the rim of bubble base (θ). The image processing procedure included the following steps: first, the wall in the raw images was removed by subtracting an image containing only the wall. Next, an intensity threshold was applied to segment the bubble from the background. Finally, V was calculated by accumulating the cross-section area at each height level from the bottom to the top of the bubble. R_a was obtained by fitting the bubble apex with a circle of radius R_a. θ was found by linearly fitting the bubble shape near the rim of bubble base. The velocity and acceleration of the bubble in the vertical direction were calculated as $U_b = dy_b/dt$ and $a_b = d^2y_b/dt^2$, where t is the time and y_b is the position of center-of-mass in the vertical direction. Assuming the uncertainty of y_b is 0.1 pixel (i.e., 3.4 μm), the uncertainty of a_b measured during the necking process is about 0.3 g.

ACKNOWLEDGMENTS

We thank the support of the National Science Foundation under grant numbers 2041479 and 2339606, UMass Dartmouth's Marine and Undersea Technology (MUST) Research Program funded by the Office of Naval Research under grant number N00014-20-1-2170, and University of Massachusetts OTCV Technology Development Fund. We also thank Paul Sousa for the assistance of fabricating the experimental setup.

CONFLICT OF INTEREST STATEMENT

The authors declare no conflicts of interest.

ORCID

Hangjian Ling https://orcid.org/0000-0001-9014-7126

REFERENCES

1. Han S, You K, Kim K, Park J. Measurement of the attachment force between an air bubble and a mineral surface: relationship between the attachment force and flotation kinetics. *Langmuir*. 2019;35:9364-9373.
2. Corbett C, Wang Q, Smith W, Liu W, Walmsley AD. Cleaning effects due to shape oscillation of bubbles over a rigid boundary. *Phys Fluids*. 2023;35:123335.
3. Shakya G, Cattaneo M, Guerriero G, Prasanna A, Fiorini S, Supponen O. Ultrasound-responsive microbubbles and nanodroplets: a pathway to targeted drug delivery. *Adv Drug Deliv Rev*. 2024;206:115178.
4. Anna SL. Droplets and bubbles in microfluidic devices. *Annu Rev Fluid Mech*. 2016;48:285-309.
5. Kumar R, Kuloor NK. The formation of bubbles and drops. In: Drew TB, Cokelet GR, Hoopes JW, Vermeulen T, eds. *Advances in Chemical Engineering*. Vol 8. Academic Press; 1970:255-368.
6. Kulkarni AA, Joshi JB. Bubble formation and bubble rise velocity in gas–liquid systems: a review. *Ind Eng Chem Res*. 2005;44:5873-5931.
7. Zhou Y, Ji B, Yan X, Jin P, Li J, Miljkovic N. Asymmetric bubble formation at rectangular orifices. *Langmuir*. 2021;37:4302-4307.
8. Hanafizadeh P, Sattari A, Hosseini-Doost SE, Nouri AG, Ashjaee M. Effect of orifice shape on bubble formation mechanism. *Meccanica*. 2018;53:2461-2483.
9. Vafaei S, Borca-Tasciuc T, Wen D. Theoretical and experimental investigation of quasi-steady-state bubble growth on top of submerged stainless steel nozzles. *Colloids Surf A Physicochem Eng Asp*. 2010;369:11-19.
10. Gnyloskurenko S, Byakova A, Nakamura T, Raychenko O. Influence of wettability on bubble formation in liquid. *J Mater Sci*. 2005;40:2437-2441.
11. Byakova AV, Gnyloskurenko SV, Nakamura T, Raychenko OI. Influence of wetting conditions on bubble formation at orifice in an inviscid liquid: mechanism of bubble evolution. *Colloids Surf A Physicochem Eng Asp*. 2003;229:19-32.
12. Gerlach D, Biswas G, Durst F, Kolobaric V. Quasi-static bubble formation on submerged orifices. *Int J Heat Mass Transf*. 2005;48:425-438.
13. Corchero G, Medina A, Higuera FJ. Effect of wetting conditions and flow rate on bubble formation at orifices submerged in water. *Colloids Surf A Physicochem Eng Asp*. 2006;290:41-49.
14. Mirsandi H, Smit WJ, Kong G, Baltussen MW, Peters EAJF, Kuipers JAM. Influence of wetting conditions on bubble formation from a submerged orifice. *Exp Fluids*. 2020;61:83.
15. Mohseni E, Chiamulera ME, Reinecke SF, Hampel U. Bubble formation from sub-millimeter orifices: experimental analysis and modeling. *Chem Eng Process Process Intensification*. 2022;173:108809.
16. Oguz HN, Prosperetti A. Dynamics of bubble growth and detachment from a needle. *J Fluid Mech*. 1993;257:111-145.
17. Qu C, Yu Y, Zhang J. Experimental study of bubbling regimes on submerged micro-orifices. *Int J Heat Mass Transf*. 2017;111:17-28.
18. Georgoulas A, Koukouvinis P, Gavaises M, Marengo M. Numerical investigation of quasi-static bubble growth and detachment from submerged orifices in isothermal liquid pools: the effect of varying

fluid properties and gravity levels. *Int J Multiphase Flow*. 2015;74:59-78.
19. Terasaka K, Tsuge H. Bubble formation at a single orifice in non-Newtonian liquids. *Chem Eng Sci*. 1991;46:85-93.
20. Rodríguez-Rodríguez J, Sevilla A, Martínez-Bazán C, Gordillo JM. Generation of microbubbles with applications to industry and medicine. *Annu Rev Fluid Mech*. 2015;47:405-429.
21. Rubio-Rubio M, Bolaños-Jiménez R, Martínez-Bazán C, Muñoz-Hervás JC, Sevilla A. Superhydrophobic substrates allow the generation of giant quasi-static bubbles. *J Fluid Mech*. 2021;912:A25.
22. Qiao S, Cai C, Chen W, Pan C, Liu Y. Control of the shape of bubble growth on underwater substrates with different sizes of superhydrophobic circles. *Phys Fluids*. 2022;34:067110.
23. Breveleri J, Mohammadshahi S, Dunigan T, Ling H. Plastron restoration for underwater superhydrophobic surface by porous material and gas injection. *Colloids Surf A Physicochem Eng Asp*. 2023;676:132319.
24. O'Coin D, Ling H. Dynamics of bubble formation on superhydrophobic surface under a constant gas flow rate at quasi-static regime. *Phys Fluids*. 2024;36:08330.
25. Mohammadshahi S, Breveleri J, Ling H. Fabrication and characterization of super-hydrophobic surfaces based on sandpapers and nano-particle coatings. *Colloids Surf A Physicochem Eng Asp*. 2023;666:131358.
26. Xu S, Wang Q, Wang N. Chemical fabrication strategies for achieving bioinspired superhydrophobic surfaces with micro and nanostructures: a review. *Adv Eng Mater*. 2021;23:2001083.
27. Mohammadshahi S, O'Coin D, Ling H. Impact of sandpaper grit size on drag reduction and plastron stability of super-hydrophobic surface in turbulent flows. *Phys Fluids*. 2024;36:025139.
28. Ling H, Srinivasan S, Golovin K, McKinley GH, Tuteja A, Katz J. High-resolution velocity measurement in the inner part of turbulent boundary layers over super-hydrophobic surfaces. *J Fluid Mech*. 2016;801:670-703.
29. Park H, Choi CH, Kim CJ. Superhydrophobic drag reduction in turbulent flows: a critical review. *Exp Fluids*. 2021;62:229.
30. Feng X, Sun P, Tian G. Recent developments of superhydrophobic surfaces (SHS) for underwater drag reduction opportunities and challenges. *Adv Mater Interfaces*. 2022;9:2101616.
31. Guan SY, Zhang ZH, Wu R, Gu XK, Zhao CY. Pool boiling inside micro-nano composite pores: thermofluids behaviors and heat transfer enhancement. *Appl Phys Lett*. 2024;124:093508.
32. Hong M, Mo D, Heng Y. Bubble dynamics analysis of pool boiling heat transfer with honeycomb micro-nano porous structured surfaces. *Int Commun Heat Mass Transfer*. 2024;152:107256.
33. Xu N, Liu Z, Yu X, Gao J, Chu H. Processes, models and the influencing factors for enhanced boiling heat transfer in porous structures. *Renew Sustain Energy Rev*. 2024;192:114244.
34. Miljkovic N, Wang EN. Condensation heat transfer on superhydrophobic surfaces. *MRS Bull*. 2013;38:397-406.
35. Chang X, Li M, Tang S, et al. Superhydrophobic micro-nano structured PTFE/WO3 coating on low-temperature steel with outstanding anti-pollution, anti-icing, and anti-fouling performance. *Surf Coat Technol*. 2022;434:128214.
36. Elius M, Richard S, Boyle K, Chang WS, Moisander PH, Ling H. Impact of gas bubbles on bacterial adhesion on super-hydrophobic aluminum surfaces. *Results Surf Interfaces*. 2024;15:100211.
37. Huang W, Huang J, Guo Z, Liu W. Icephobic/anti-icing properties of superhydrophobic surfaces. *Adv Colloid Interface Sci*. 2022;304:102658.
38. Latthe SS, Sutar RS, Bhosale AK, et al. Recent developments in air-trapped superhydrophobic and liquid-infused slippery surfaces for anti-icing application. *Prog Org Coat*. 2019;137:105373.
39. Mohamed AMA, Abdullah AM, Younan NA. Corrosion behavior of superhydrophobic surfaces: a review. *Arabian J Chem*. 2015;8:749-765.
40. Xiang T, Han Y, Guo Z, et al. Fabrication of inherent anticorrosion superhydrophobic surfaces on metals. *ACS Sustain Chem Eng*. 2018;6:5598-5606.
41. Ling H, Katz J, Fu M, Hultmark M. Effect of Reynolds number and saturation level on gas diffusion in and out of a superhydrophobic surface. *Phys Rev Fluids*. 2017;2:124005.
42. Nosrati A, Mohammadshahi S, Raessi M, Ling H. Impact of the under-saturation level on the longevity of superhydrophobic surfaces in stationary liquids. *Langmuir*. 2023;39:18124-18131.
43. Bourgoun A, Ling H. A general model for the longevity of super-hydrophobic surfaces in under-saturated, stationary liquid. *J Heat Transfer*. 2022;144:042101.
44. Ma J, Li J, Zhou P, Song Y, Chai L, Zhou CQ. A viewpoint on the dynamics of bubble formation from a submerged nozzle. *Eur J Mech B Fluids*. 2019;78:276-283.
45. Tate T. On the magnitude of a drop of liquid formed under different circumstances. *London, Edinburgh Dublin Philos Mag J Sci*. 1864;27:176-180.
46. Burton JC, Waldrep R, Taborek P. Scaling and instabilities in bubble pinch-off. *Phys Rev Lett*. 2005;94:184502.
47. Keim NC, Møller P, Zhang WW, Nagel SR. Breakup of air bubbles in water: memory and breakdown of cylindrical symmetry. *Phys Rev Lett*. 2006;97:144503.
48. Thoroddsen ST, Etoh TG, Takehara K. Experiments on bubble pinch-off. *Phys Fluids*. 2007;19:042101.
49. Quan S, Hua J. Numerical studies of bubble necking in viscous liquids. *Phys Rev E*. 2008;77:66303.
50. Loubière K, Hébrard G. Bubble formation from a flexible hole submerged in an inviscid liquid. *Chem Eng Sci*. 2003;58:135-148.
51. Di Bari S, Robinson AJ. Experimental study of gas injected bubble growth from submerged orifices. *Exp Therm Fluid Sci*. 2013;44:124-137.
52. Vafaei S, Angeli P, Wen D. Bubble growth rate from stainless steel substrate and needle nozzles. *Colloids Surf A Physicochem Eng Asp*. 2011;384:240-247.
53. Zhu D, Song Y, Gao F, et al. Achieving underwater stable drag reduction on superhydrophobic porous steel via active injection of small amounts of air. *Ocean Eng*. 2024;308:118329.
54. Cho W, Heo S, Lee SJ. Effects of surface air injection on the air stability of superhydrophobic surface under partial replenishment of plastron. *Phys Fluids*. 2022;34:122115.
55. Qin S, Fang H, Sun S, Wang X, Cao L, Wu D. Fabrication of air-permeable superhydrophobic surfaces with excellent non-wetting property. *Mater Lett*. 2022;313:131783.
56. Li Z, Marlena J, Pranantyo D, Nguyen BL, Yap CH. A porous superhydrophobic surface with active air plastron control for drag reduction and fluid impalement resistance. *J Mater Chem A Mater*. 2019;7:16387-16396.

SUPPORTING INFORMATION

Additional supporting information can be found online in the Supporting Information section at the end of this article.

How to cite this article: O'Coin D, Ling H. Effect of gas flow rate on bubble formation on superhydrophobic surface. *Droplet*. 2025;e148. https://doi.org/10.1002/dro2.148